Spalling Hazard Occurrence in Longwall Excavation: a Case Study

Sunny Murmu[1] · Gnananandh Budi[1]

Abstract

One of the most significant concerns in longwall ground control is the instability and failure mechanism of the coal wall. The current research uses FLAC^{3D} to simulate panel 1 of the Adriyala Longwall Project, India, in order to evaluate the distribution of vertical stress and material failure mode, in and around the longwall face. Additionally, three distinct criteria are used to evaluate coal wall spalling: vertical stress distribution, maximum shear strain, and residual cohesion. A novel algorithm is also proposed to appropriately capture roof bed caving, shield installation and advancement, and coal extraction from the face. The findings of the modelling show that progressive longwall extraction creates an elliptical stress relief zone around the excavation void. During the peak stress phase, the height of the stress relief zone is greatest, whereas the width is highest during the main fall phase. As mining advances, the coal wall at the face line appears to lose its stress-bearing capability. Shear failure was the most common coal wall failure mode. Maximum spalling depth (MSD) and longwall face spalling index (LFSpI) were used to measure the extent and volume of coal wall spalling in FLAC^{3D}. For panel 1 of the ALP mine, the MSD, and LFSpI were determined to be 3 m and 90.5 %, respectively. The mode of coal wall spalling was expected to be total or fragmented failure. The field observations and the numerical modelling findings were in good agreement. The compressive strength and deformation modulus of the immediate roof appear to have a substantial role in coal wall spalling. The results of the proposed numerical simulation exercise can help strata control engineers better detect the risks of coal wall spalling and enhance face control for safe and productive working environment at the longwall face.

Keywords Geomechanics · Spalling of coal wall · FLAC^{3D} · Longwall face failure · Stress distribution

1 Introduction

Spalling of the coal wall has become a serious ground control issue in longwall panels operating in subcritical conditions. It is also known as face rib spalling or face sloughage. It is the dislodgement, detachment of massive slabs or flow of large-scale small fragmented coal from the coal wall into the working face with little or no warning [1]. It results from a complex interaction between the coal wall, roof strata, floor, and shield support. Typically, it is caused by the face instability condition triggered by loss of confinement at the coal wall's perimeter and high abutment stress ahead of the coal wall in subcritical panels working at greater depth. As the face advances, the in situ stresses are redistributed, resulting in the formation of abutments near the excavations' boundaries. The abutment stress front of the coal wall is often high in magnitude, resulting in either tensile failure for brittle rock or shear failure for soft or weak rock [2]. The coal wall in the vicinity of the face experiences failures developing shear and tensile cracks (localization of plastic deformation) under the influence of a high magnitude of abutment stress greater than its strength. Several cracks coalesce together to form a major plane of weakness, causing the slab to either slide or split out of the coal wall. Furthermore, the failure of a coal wall can result in the formation of numerous cracks with high plastic flow, resulting in spalling in the form of debris flow or large-scale small fragmented flow. It often occurs in the middle of the face or at the corners where gate roads intersect; however, it can occur anywhere along the face line, placing machinery and human resources at risk.

✉ Sunny Murmu
   sunny.murmu1@gmail.com

   Gnananandh Budi
   anandbudi@iitism.ac.in

1 Department of Mining Engineering, Indian Institute
   of Technology (Indian School of Mines), Dhanbad 826004,
   India

Longwall mining causes extensive scale caving of roof strata. Suppose the influence of geological anomalies such as faults, dirt bands, or sandstone channels is not being considered. In that case, a strata control engineer might expect the extent and severity of coal wall spalling to be the most significant during the main weighting period instead of the periodic weighting period or normal cycle. The magnitude of caving and the degree of failure at the longwall face were found to be highly correlated [3]. Furthermore, until the main weighting period, the gob formation is incapable of bearing the partial load of the overlying strata [4]. As a result, maximal load transfer is achieved at the face. The progressive retreat of the longwall face causes front abutment stress to build ahead of the coal wall. Prior to the main roof rupturing, the front abutment stress reaches its maximum magnitude. As a result, shear or lateral strains in the coal wall reach their maximum. Spalling begins when a significant quantity of plastic flow is generated in the coal wall.

The impetus for roof falls at the unsupported span of the longwall face is frequently attributed to coal wall spalling [2]. It tends to increase the tip-to-face distance, putting the roof's stability at risk ahead of the canopy's tip. The formation of a roof cavity at the unsupported span causes coal dilution and necessitates the installation of a false roof, limiting the shields' effectiveness. Face failures are detrimental and can cause major difficulties such as overloading and blocking of AFC, damage to face equipment, dust generation, ore dilution, risk to mine personnel, and even iron bounding of shields in cases where the coal seam and immediate roof are both soft in nature [5]. As a result, several issues and redundant tasks arise, such as production delays, manual handling, and the need for secondary blasting of large coal lumps, preparation of artificial roof for proper shield setting, and additional maintenance of face equipment. Spalling of the face is responsible for approximately 8% of all casualties in the USA [6]. Recovering from such failures is a time-consuming and costly process. Furthermore, the techno-economic benefits of longwall mining are impeded as a result of slower face progress and lower productivity. Hence, the coal wall's structural stability is extremely crucial.

1.1 Types of Coal Wall Failure

The coal wall has three primary modes of failure: (a) shear failure, (b) tensile failure, and (c) buckling failure (Fig. 1a–c). The structural development of fractures in the coal wall under high abutment stress causes the most of coal wall spalling to occur in shear failure mode. Tensile failure is uncommon; however, it is frequently associated with a hard coal wall with a compressive strength greater than 40 MPa. This sort of coal wall has brittle post-peak behaviour rather than progressive strain softening. Buckling failure mode in coal walls is more common on large-heighted faces (> 4 m). However, the types of coal wall failure are not limited to the ones listed above. It varies greatly depending on the geological context of the surrounding strata and the coal wall's geotechnical properties. Coal wall failures can be further classified as (a) upper failure, (b) central failure, (c) integral failure, (d) lower failure, (e) total failure, and (f) fragmented failure (Fig. 2). The top section of the coal wall is more prone to upper failure because of stress concentration at this junction. The coal wall is stressed as a result of the roof deformation. When the stress exceeds the coal wall's bearing capacity, it fails, resulting in upper failure. The failure mode in a competent coal wall is blocky because the fracture growth is prominent and in the direction of a localised deformation zone. This form of failure is strength controlled. The risk to workers and equipment is significant. In soft seams with pre-existing joints, such as cleat fractures, form randomly. Under these conditions, the abutment stress development is highly unequal. Small blocks are formed by the distribution of fractures. Small blocky kind of coal wall spalling is noticed when these cracks dilate. This sort of coal wall collapse is fracture controlled. In the case of significant horizontal stress, the floor buckles or heaves into the longwall face, imparting pressure at the coal wall bottom leading to lower failure. If the roof deformation and floor heaving take place simultaneously, stress concentration zones form at the top and bottom of the coal wall, resulting in total failure. The fundamental mechanistic causes are the
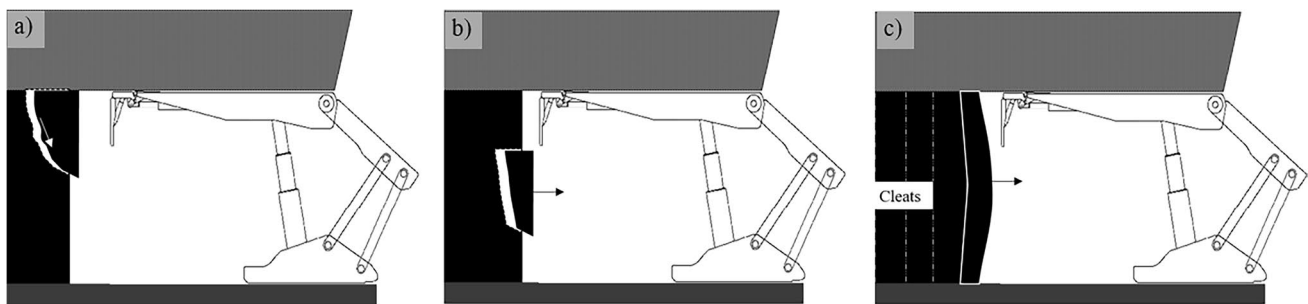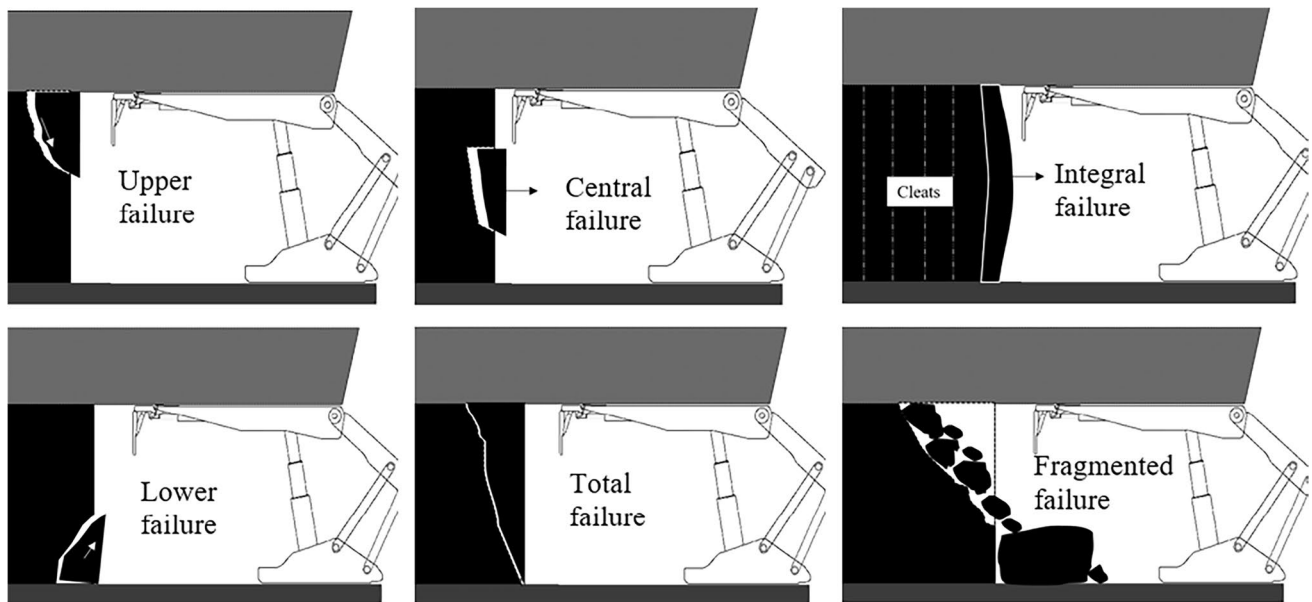

Fig. 1 Basic type of coal wall spalling

Fig. 2 Variants of coal wall spalling

same for integral and total failure of a coal wall. The presence of near vertical cleats and the considerable height of the coal wall are the only differences. Central failure occurs when a section of the coal wall extrudes from the centre owing to tensile stress. A common type of coal wall failure is the fragmented failure observed in longwall operations under large cover depth (> 400 m). In this sort of failure, the yield zone extends far forward into the coal wall. The volume of spalled coal in debris form is so huge that mining equipment or even workers may become buried beneath it. This is owing to significant abutment stress generation and high extent of yield zone in the coal wall as a result of the deep cover. In this form of failure, the structural failure of the seam is considerable.

1.2 Previous Studies

Studies to understand the fundamental geomechanics of coal wall spalling have been attempted in the past. The US Bureau of Mines began by investigating the causes and effects of coal wall spalling using fundamental mechanical theoretical equations. They emphasized that mining depth and extraction height are two key factors influencing coal wall spalling. Furthermore, the coal seam's friability and cleat orientation were deemed critical variables [1]. Most research on coal wall spalling has been on faces associated with large-cutting-height (LCH) or longwall top coal cavability (LTCC) longwall extraction techniques. Yong et al. assessed rib spalling of high coal walls in fully mechanised mines using theoretical damage mechanics [7]. Coal wall spalling has been assessed using theoretical models such as

the limit equilibrium approach and Winkler's elastic beam foundation model [8–13]. The mechanism of fracture development at the coal front was also investigated using physical models [12, 14–17]. The majority of numerical modelling research looked at how shield properties, operating factors, and coal seam characteristics affected coal wall spalling [2, 5, 18–20]. Yao et al. looked into the influence of seam dip on the coal wall and the resultant fracture progression [21]. Spalling of coal wall was also investigated under a massive sandstone key roof [22].

Previous research has found that the extent and severity of coal wall spalling are influenced by the geomining condition, physico-mechanical properties of the rock beds, panel geometrical parameters, in situ stress regime, powered support characteristic, structural discontinuities, panel operational parameters, presence of ground water, and geological anomalies. However, just a few of the parameters have been studied, including shield characteristics, advance rate, depth, and coal seam characteristics. Furthermore, there is yet to be an assessment of coal wall spalling during the main weighting period (MWP), when it is most severe. As a result, the goal of this research is to conduct a detailed numerical analysis of coal wall spalling during the MWP in a longwall panel. For continuum-based numerical analysis codes, a novel set of spalling estimate criteria is provided. After that, field-measured parameters are used to calibrate the numerical model. The calibrated model is then used to investigate stress distribution, rock mass failure, and strata caving around the excavation in considerable detail. Following that, the influence of geotechnical characteristics of the immediate and main roof on coal wall spalling is investigated.

2 Background of Longwall Mine Under Study

2.1 Geological Setting

The Adriyala Longwall Project (ALP) is located in the Godavari Valley Coalfields' Ramagundem coal belt in Telangana's Karimnagar District, southeast to Singareni Collieries Company Limited's current GDK10A mine in the Ramagundem-II region (Fig. 3). The project has a total reserve of 78.597 million tonnes, with depths ranging from 294 to 644 m. Major geological discontinuities are sparse in AL's geological block. North latitude 180° 39′ 03″ to 180° 40′ 34″ and East longitude 790° 34′ 28″ to 790° 35′ 55″ define the boundaries of ALP, which spans 3.4 km². Only four of the seven coal seams in the lease area are considered viable for mining, namely I, II, III, and IV. The project has a 35-year life cycle and a 2.817 million tonne per year production target. Accordingly, four panels have been proposed for the mining of the coal reserve from seam I in ALP, namely panels 1–4 (Fig. 4). Geotechnical data from six boreholes, namely 1203, 1199, 1205R, 1198A, 1196A, and 1210, are

used to examine the cavability of the overlying roof rocks of the No. 1 seam. The lithology of several boreholes was studied in order to determine the primary parting planes overlying the seam and to estimate the immediate and main roofs in the various boreholes in order to acquire a sense of strata variation over the coal seam. The results of the boreholes are summarised in Table 1. The depth and thickness of seam I vary from 361 to 543 m and 5.7 to 6.5 m, respectively, as shown in Table 1. Shaly coal and carbonaceous shale with thicknesses varying from 2.4 to 12.5 m comprise the immediate roof. Since the extraction height of seam I has been set at 3.5 m, a significant thickness of inferior coal of more than 2.5 m forms part of the immediate roof. The main roof comprises of coarse- to fine-grained grey sandstone with a massive thickness of 14–26.5 m. Because of its close proximity to the seam, it is the dominating unit and plays a significant role in weighing events and load transfer to the face. Figure 5 shows the stratigraphic sequence of the layers overlying the seam I. Panel 1 (P1), 50 m wide and 2350 m long with a depth of cover ranging from 380 to 506 m, is the subject of the present scientific investigation. The thickness of seam I in P1 varies from 5.9 to 6.5 m. Only the lowest section (3.5
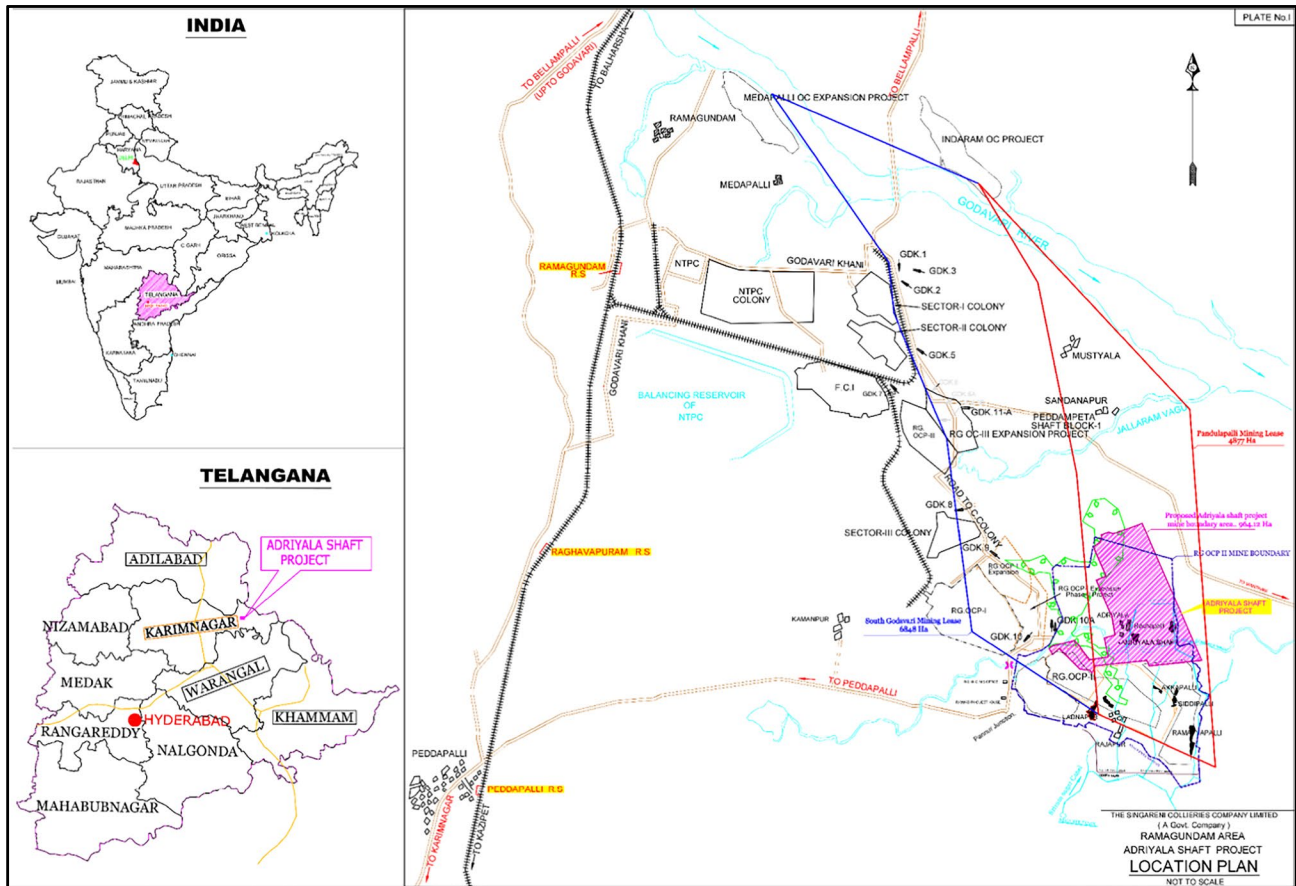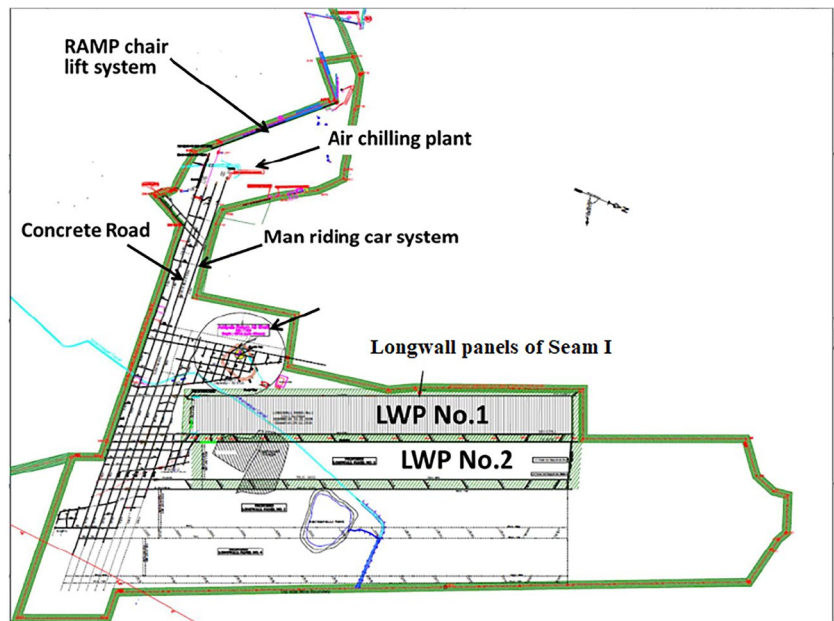

Fig. 3 Location plan of Adriyala Longwall Project mine

Fig. 4 Key plan of longwall panels in ALP

Table 1 Borehole log lithology summary of ALP

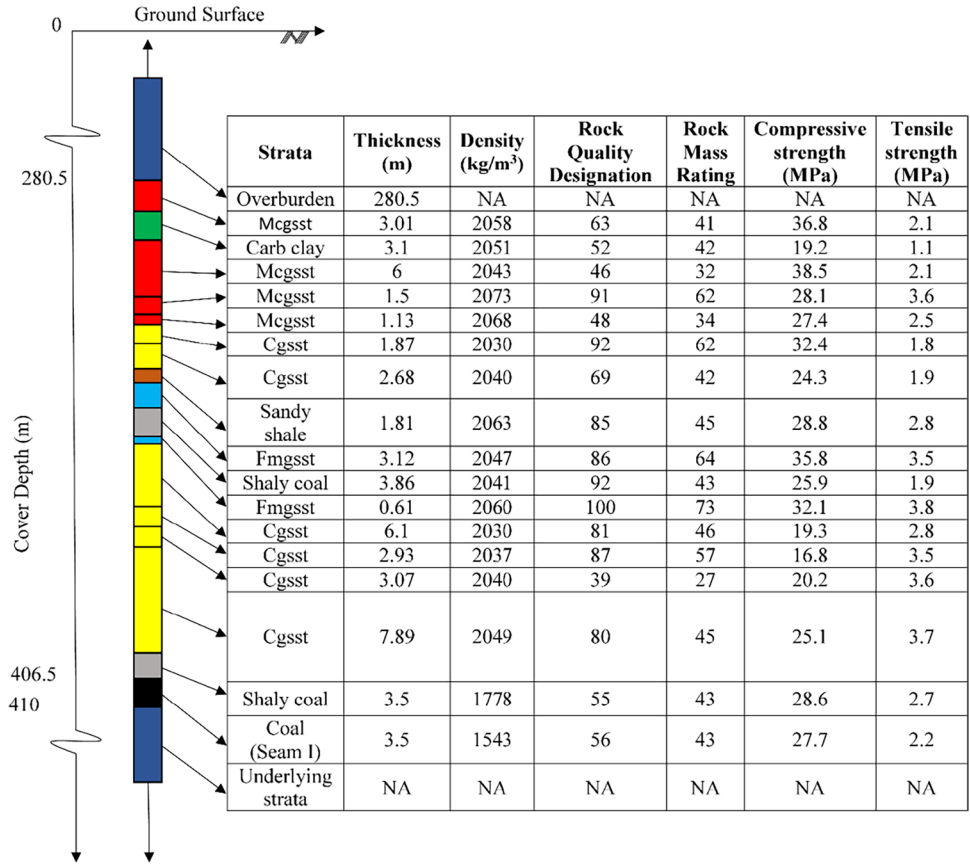| Bore hole No.	Location	Average depth (m)	Average seam thickness (m)	Immediate roof thickness (m)	Main roof thickness (m)	Parting planes above seam (m)
1203	Near the start along the central line of panel 1	361	5.9	4.3	14.3	21, 28, 48
1199	Approximately 100m along the central line of the panel 1	375	5.9	2.4	21.4	25, 28, 32, 48
1205R	At the middle of the panel 1	391	6.5	7	24.3	25, 32, 47
1198A	At the middle of panel 1 along the central line	406.5	3.5	3.5	20.5	24, 31, 46
1196A	At the end of panel 1	422	6.3	12.5	17	34, 36, 41
1210	Near the mine boundary at the start of panel 4	543	6.1	3.6	26.5	30

m) of the seam is being mined since the upper half is made up of two clay bands. P1 has single-entry gate road that is 5.2 m wide. The width of chain pillars varies from 45 to 55 m. In P1, 146 shield supports of 2 × 11,300 kN have been installed. The average daily rate of progress was 4.25 to 5.1 m, according to reports.

2.2 Strata Behaviour and Coal Wall Spalling Related Parameters as Observed in the Field

Over a 5-day period, the first significant main roof weighting or main weighting period (MWP) for panel 1 of ALP was observed between 77 and 83 m of face retreat from the setup room. The area of fall covered during the primary weighing was 23,205 m². Just before the mainfall (i.e. 83 m face retreat) of the caving main roof, a significant convergence of 36 mm/day was recorded in the main gate. The maximum cumulative convergence recorded by dual height tell-tale convergence metre was 112 mm

(Fig. 6). There were around 115 shield legs within the weighted zone. Approximately 90 shields out of 146 (total no. of shields across the longwall face) yielded during the MWP. From the 43rd to the 134th shield, the weighing zone was extended, i.e. approximately 160 m (Fig. 7). The occurrence of coal wall spalling across the face in the series of the placement of the shields was monitored during the weighting events. Between the 40th and 114th shields, there was significant coal wall spalling, i.e. approximately 130 m (Fig. 8). The longwall face was severely damaged by spalling that reached a depth of around 3 m into the coal wall (Fig. 9). The height of the spalling was almost touching the roof and the floor. Towards the roof the area of spalling was large and gradually tapered down towards the floor. The abutment zone ahead of the face was almost 26 m, according to the stress cell installed within the chain pillar at 6 m depth and 80 m from the setup room (Fig. 10). During the extraction of P1, the mine's subsidence was

**Fig. 5** Stratigraphic sequence of rock beds in ALP

Strata	Thickness (m)	Density (kg/m³)	Rock Quality Designation	Rock Mass Rating	Compressive strength (MPa)	Tensile strength (MPa)
Overburden	280.5	NA	NA	NA	NA	NA
Mcgsst	3.01	2058	63	41	36.8	2.1
Carb clay	3.1	2051	52	42	19.2	1.1
Mcgsst	6	2043	46	32	38.5	2.1
Mcgsst	1.5	2073	91	62	28.1	3.6
Mcgsst	1.13	2068	48	34	27.4	2.5
Cgsst	1.87	2030	92	62	32.4	1.8
Cgsst	2.68	2040	69	42	24.3	1.9
Sandy shale	1.81	2063	85	45	28.8	2.8
Fmgsst	3.12	2047	86	64	35.8	3.5
Shaly coal	3.86	2041	92	43	25.9	1.9
Fmgsst	0.61	2060	100	73	32.1	3.8
Cgsst	6.1	2030	81	46	19.3	2.8
Cgsst	2.93	2037	87	57	16.8	3.5
Cgsst	3.07	2040	39	27	20.2	3.6
Cgsst	7.89	2049	80	45	25.1	3.7
Shaly coal	3.5	1778	55	43	28.6	2.7
Coal (Seam I)	3.5	1543	56	43	27.7	2.2
Underlying strata	NA	NA	NA	NA	NA	NA

monitored on a regular basis from the subsidence pillars constructed at the ground surface in 30 m grid pattern. When the panel extraction reached 350 to 400 m, which is equal to the average depth of the panel, subsidence was first noticed. The maximum subsidence of 2.1 m was reported at a monitoring location of 592 m along the panel length (Fig. 11). The strata movement of distinct beds was recorded using a multipoint borehole extensometer (MPBX) positioned at 1700 m from the setup room.

MPBX monitoring points were embedded into the ground at various depths from the surface, namely 70 m, 290 m, and 350 m, respectively. When the longwall face was at a distance of approximately 35 m from the MPBX position, bed separation was noticed. When the face crossed the MPBX site, there was a rapid rise in the downward displacement of all three monitoring stations. The highest downward movement was 0.552 m at the 350 m embedded monitoring site (Fig. 12).
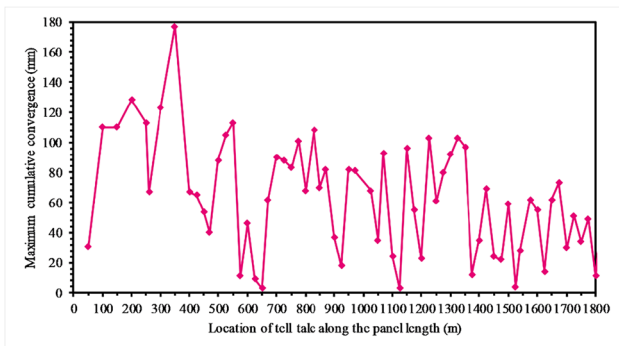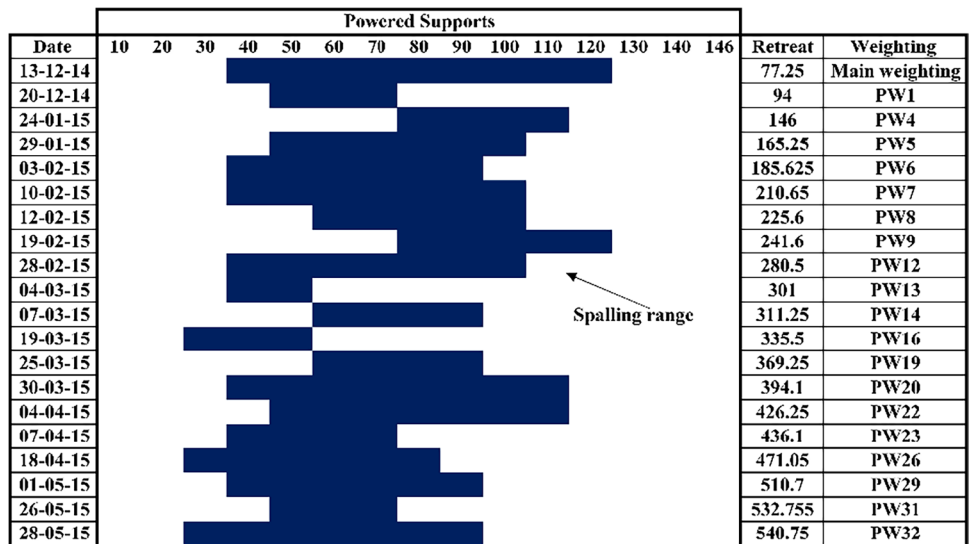
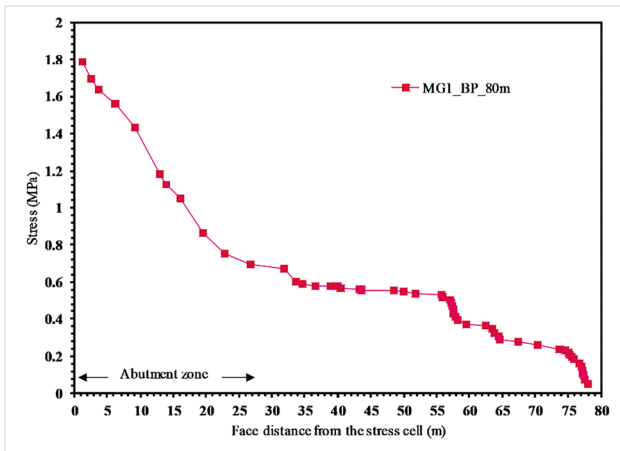**Fig. 6** Maximum cumulative convergence measured along the gate road
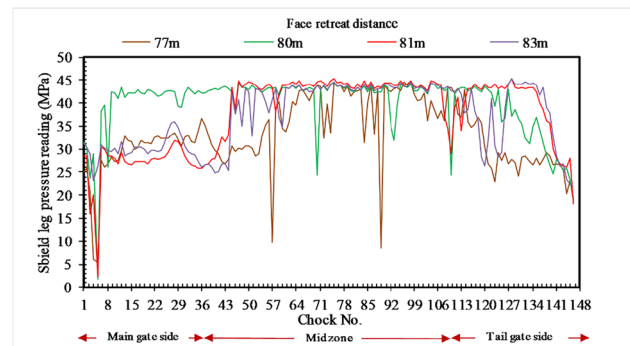
Fig. 7 Recorded shield pressure reading during the main weighting period
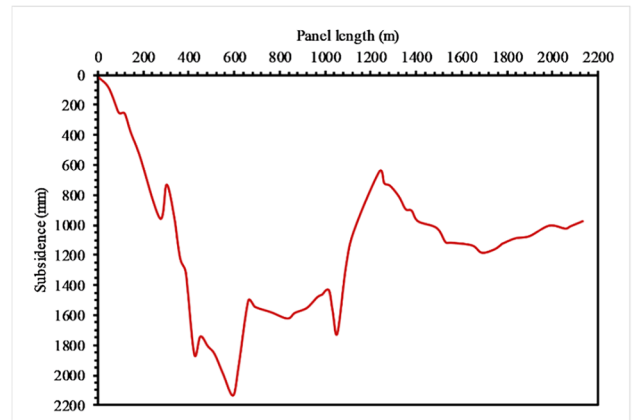
Fig. 8 Spalling across the location of shield supports

Fig. 9 Spalling of coal wall in ALP, panel 1 during MWP

Fig. 10 Stress cell reading recorded for mining progress at ALP, panel 1

Fig. 11 Subsidence recorded at the ground surface above panel 1 of ALP
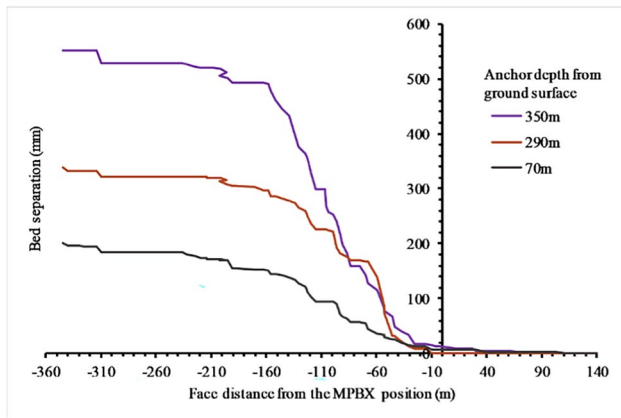
Fig. 12 Bed separation observed in the overburden layers due to caving of strata

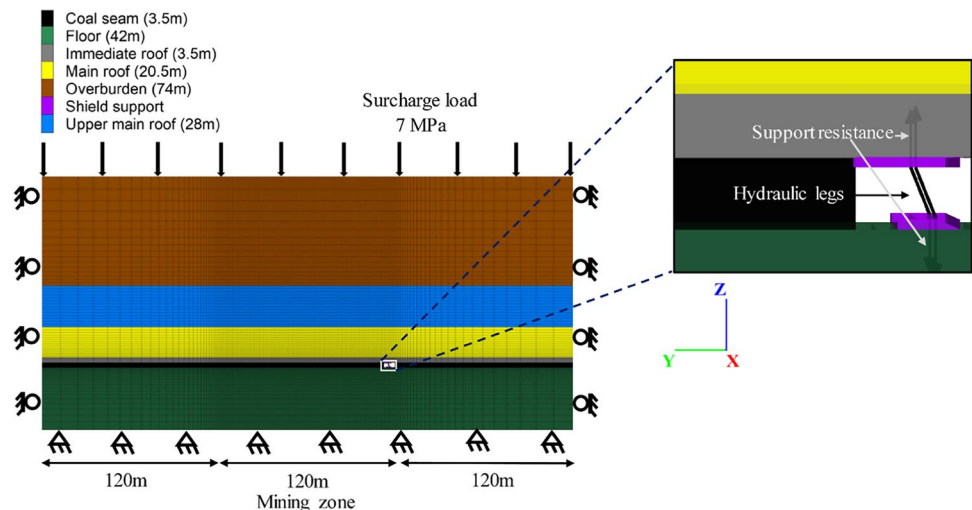# 3 Numerical Modelling Procedure

3.1 Model Geometrical Configuration

The FLAC^{3D} code was employed in this investigation to simulate non-linear material behaviour, complex geometries, and sophisticated steps like progressive failure and caving of strata. FLAC^{3D} has proven to be a suitable tool for modelling longwall panel rock mass behaviour [18–20, 23–25]. The middle component of the panel, consisting of one shield in the longitudinal direction, was simulated to avoid computational difficulties caused by geometric complexity, long solution times, and huge memory allocation. The model's length in the Y direction was 360 m, with the centremost 120 m designated as a mining zone, and adequate space was left on both sides to avoid boundary influences changing the results. The model's width in the X direction was 1.75 m, which was the same as the shield's width. In the Z direction, the overall

height includes the floor (42 m), seam (3.5 m), immediate roof (3.5 m), main roof (20.5 m), upper main roof (28 m), and overburden (74 m). A finer meshing was investigated at the desired area of interest. The size of the zones steadily expanded as one got closer to the border (Fig. 13). For the seam, the total cover depth is considered to be 406.5 m. A uniform vertical stress magnitude of 7 MPa was applied to the top of the model to compensate for the portion of the roof layers that were not modelled considering an average unit weight of the strata as 0.025 MN/m^3. A gradient mean horizontal stress was applied to both sides of the model in the longitudinal direction. The mean in situ horizontal stress value was calculated using Sheorey's empirical equation [26]. Many researchers employ Sheorey's stress theory (Eq. 1) because it provides a reasonable approximation of mean horizontal stress in the absence of measured in situ stresses [4, 27].

$$\sigma_H = \sigma_h = \frac{v}{1-v}\sigma_V + \frac{\beta EG}{1-v}(H + 1000) \tag{1}$$

where σ_H is the major horizontal stress (MPa), σ_h is the minor horizontal stress (MPa), E is Young's modulus, v is Poisson's ratio, β is the coefficient of thermal expansion (/°C), G is the geothermal gradient (°C/m), H is the depth of cover (m), and σ_V is the vertical in situ stress (MPa). The bottom of the model was fixed, and in the longitudinal and transverse direction, a roller-supported boundary condition was applied to both sides of the model. The canopy and base of the shield were created utilising eight node hexahedron brick shaped elements. The canopy and base were 5 m × 1.75 m and 3 m × 1.75 m in size. Beam elements were used to model the shield's legs. A linear elastic constitutive approach was utilised to simulate the behaviour of the powered support under roof loading. For the shield, 210 GPa and 0.3 were chosen as the typical mild steel elastic modulus

Fig. 13 Numerical model geometry and its associated configuration

Beds	Thickness (m)	Density (kg/m³)	Bulk modulus (GPa)	Shear modulus (GPa)	Tensile strength (MPa)	Compressive strength (MPa)
Overburden	74	2046	1.7	1	0.3	9.7
Upper main roof	28	2048	1.9	1.2	0.3	11.8
Main roof	20.5	2041	2.6	1.6	0.5	10.5
Immediate roof	3.5	1778	1.1	0.6	0.3	4.5
Seam	3.5	1543	0.9	0.6	0.3	4.5
Floor	42	2081	2.1	1.2	0.5	17.6

Table 2 Rock mass properties taken as input for numerical simulation

and Poisson's ratio [2]. The yield capacity of each leg of the shield was defined at 5.2 MN. The set capacity was 60 % of the yield capacity and was applied as structurally applied force by the legs at the grid points connecting the canopy and base. The load on the support evolved as a result of the roof-to-floor convergence and the hydraulic leg stiffness.

3.2 Rock Mass Properties Estimation

The input in the form of rock unit physico-mechanical characteristics has a significant impact on the numerical modelling results. Consequently, firstly, the intact rock characteristics for the rock units were determined in the laboratory using geotechnical testing of a newly collected core specimen in accordance with ISRM recommendations. In addition, to account for the reduction in strength attributed to the presence of discontinuities, the geotechnical parameters of the intact rock

must be scaled to rock mass. Therefore, Zhang's approach (Eqs. 2 and 3) for determining the deformation modulus and compressive strength of a rock mass by scaling the intact rock elastic modulus and compressive strength using rock quality designation (RQD) was put into practice [28, 29].
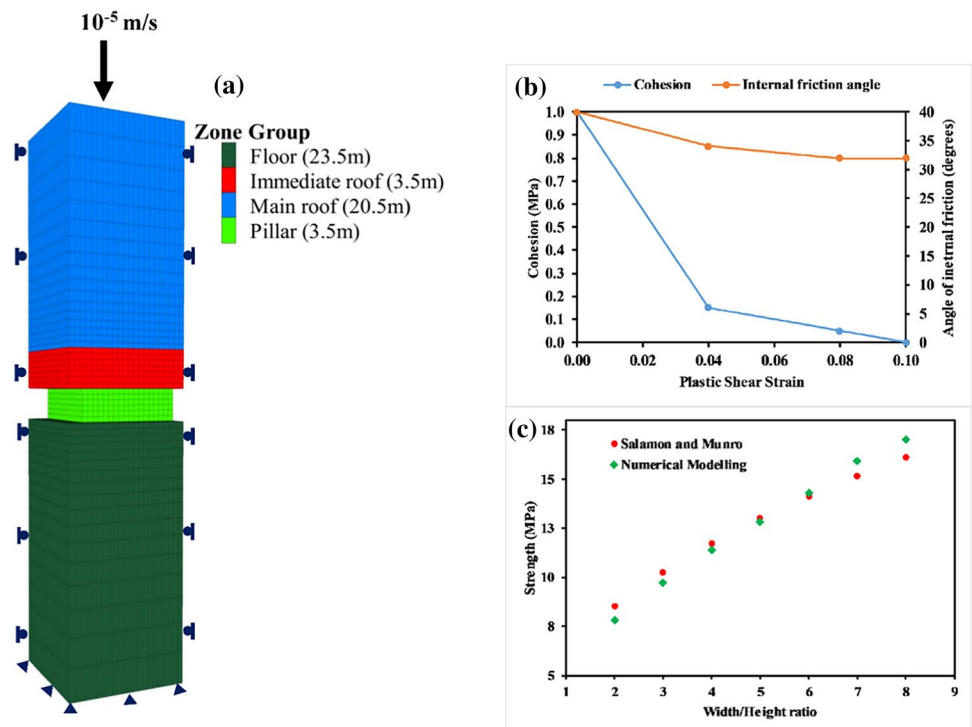
$$\frac{E_{rm}}{E_i} = 1.8 * 10^{0.0186RQD-1.91} \tag{2}$$

where E_{rm} and E_i are the deformation moduli of rock mass and intact rock.

$$\frac{\sigma_{cm}}{\sigma_i} = 10^{0.013RQD-1.34} \tag{3}$$

where σ_{cm} and σ_i are the compressive strength of rock mass and intact rock. Table 2 shows the rock mass parameters of rock beds that were obtained and used as input for modelling.

Fig. 14 Strain-softening parameter calibration

3.3 Constitutive Models for Simulating Rock Behaviour

Since the failure process of rocks consists of three distinct stages: elastic, plastic softening/hardening, and residual, the elasto-plastic material behaviour was taken into account for all rock units in the numerical model. The caving zone of the panel, according to Peng (2006), is six to seven times the extraction height. As a result, a strain-softening constitutive model with progressive plastic strain was utilised for the height of caving and the seam. For the floor and overburden, however, the Mohr-Coulomb perfectly plastic constitutive model was used. A coal pillar sub-model with roof and floor up to 24 m on either side was built to calibrate the strain-softening input parameters by the performing uniaxial compressive strength (UCS) test (Fig. 14a–c). In the coal pillar's UCS test, the roof and floor served as loading platons. In this study, changing the width-to-height ratio while applying servo-controlled velocity (10^{-5} m/s) over a flat square pillar with quarter symmetry has been used in a number of UCS experiments. Several cohesion and friction drop trials were performed with plastic strain increment, and the pillar strength obtained was compared to Salamon and Munro's pillar strength formula as shown in Eq. 4 [30]. The pillar strength formula shown in Eq. 4 has been derived after statistical analysis of data pertaining to 98 stable and 27 collapsed cases of coal pillar in the South African coal fields. Statistical analysis is an important tool for model development [31–33].

$$S_p = 7.716 \frac{W^{0.46}}{H^{0.66}} \; (MPa) \qquad (4)$$

As the width-to-height ratio rises, so does the peak strength. The rate of cohesion and friction drop, as well as a comparison of pillar peak strength obtained from simulation and Salamon and Munro's equation, is shown in Figure 14a, b, and c. It can be observed that the model findings and empirical strength have come to a reasonable agreement. As a result, the input properties shown in Fig. 14a may be utilised to simulate the rock strata's strain-softening behaviour.

3.4 Progressive Face Advancement, Powered support, and Roof Caving Algorithm

In order to initialise the in situ vertical and horizontal stresses, the model geometry was elastically solved first. The powered support was then installed, with support resistance regulated by roof convergence and leg stiffness, in an 8 m cut that represented a setup room. After that, the longwall panel was extracted in phases, each with a 1 m face advance, until the main weighing period came to an end. To manage the

progressive extraction of the seam and the cyclic installation of powered support, several FISH scripts were implemented. After each step of excavation, a separate FISH routine was implemented to check if the roof had caved in. Yielding or failure of roof is a pre-requisite for caving. Caving, on the other hand, involves more than just yielding. Caving is not the same as yielding. The overlying roof was found to have yielded in shear and tension. The removal of rock blocks from the overlying roof is required for caving. Version 6 of FLAC^{3D} does not include a built-in constitutive model for simulating caving. Critical values of plastic shear strain, ε^s (0.25) and plastic tension strain, ε^t (0.05) were determined to designate the caved zones. Furthermore, a critical threshold for the roof to cave was set at 0.4 m vertical displacement (d_v). When a zone meets the criteria to be caved, it is nulled (Fig. 15). These parameters were intuitively selected after
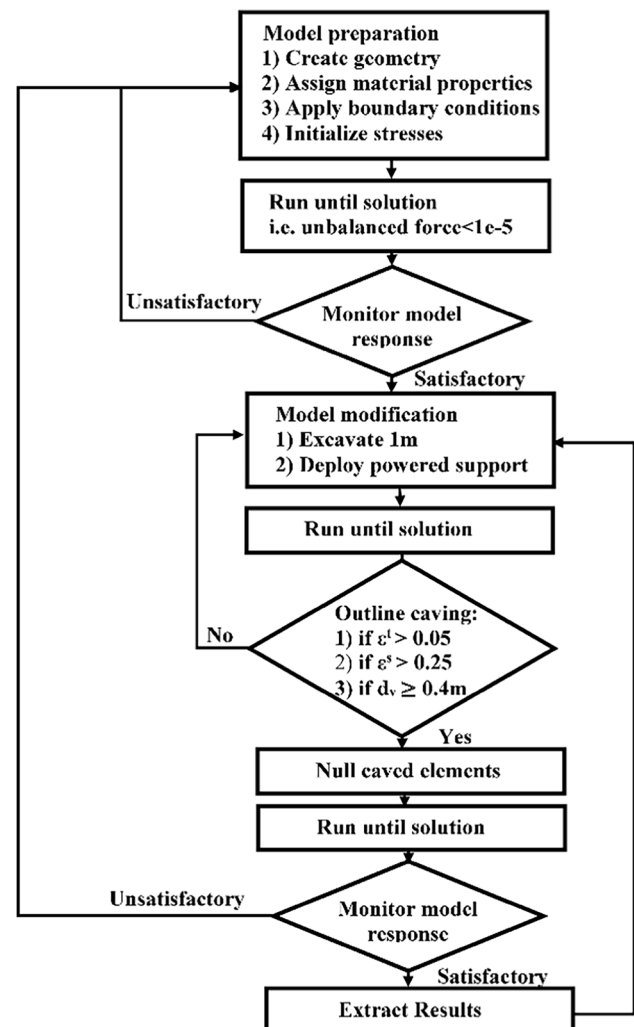

Fig. 15 Algorithm for coal excavation, shield installation and advancement, and caving of strata

several simulation attempts. For roof caving in longwall panels, other studies used a similar strategy [34–37].

3.5 Coal Wall Spalling Estimation Indicators and Model Calibration

The FLAC^{3D} code does not explicitly provide a facility for estimating coal wall spalling. Consequently, three indicators were utilised to delineate the region of spalling in the coal wall at the longwall face: (1) vertical stress distribution, (2) residual cohesion, and (3) maximum shear strain. Due to extensive damage induced by loss of confinement and high abutment experiences, the region of possible spalling in the coal wall has a minimal load bearing capacity. The rock strength characteristics in this area have deteriorated significantly and irreversibly. The gradual rising or near horizontal slope of the vertical stress distribution in the coal wall distinguishes the area of low load-bearing capacity. There is a significant drop in cohesion when the coal wall fails owing to its strain-softening post-peak behaviour. A typical shear test of a rock specimen suggests that after fracturing, the specimen loses cohesion along the fracture and its residual strength is mainly due

maximum extent of spalling potential that can develop ahead of the longwall face is measured by MSD. The depth of spalling may be equal to the MSD value if the MSD value is small. However, just because the MSD number is high does not automatically imply that the coal wall will extrude out at once as per the value of MSD. The major purpose of MSD is to define the maximum extent of the extremely unstable and prone to spalling region in front of the face. The LFSpI is a function of the spalled volume of the coal wall and hence explains the various modes of coal wall spalling. LFSpI can be calculated as follows:

The modes of coal wall spalling failure can be explained from the following Table 3. A low MSD value indicates a generally stable coal wall, whereas a high MSD value indicates a disturbed and unstable coal wall with the potential for extensive spalling. However, it must be seen in tandem with LFSpI in order to reliably conclude that the face is highly unstable. High LFSpI values do not always imply increased spalling. However, a high MSD in combination with a high LFSpI indicates a highly fractured zone with high proneness to spalling. Therefore, it is advised that both criteria

$$LFSpI = \left(\frac{\text{no.of elements within the area of coal wall having maximum shear strain} > 0.09}{\text{total no.of elements in that area}} \right) * 100\% \qquad (4)$$

to friction across the fracture surface. As a result, a simple criterion is provided for determining the zone of coal wall spalling by assessing modelling elements with minimal cohesion. Furthermore, in damaged rock mass, the accumulation of irreversible plastic strain is substantially higher. Intense fracture is indicated by the high maximum shear strain localisation inside the coal wall.

Two terminologies have been used to describe the depth and shape of coal wall spalling: (a) maximum spalling depth (MSD) and (b) longwall spalling index (LFSpI). The

be used in combination for a comprehensive assessment of coal wall spalling.

The shape of the maximum shear distribution in the coal wall was considered as the primary source of inference for understanding the different modes of coal wall spalling failure. If the shape and distribution of maximum shear strain are uniformly distributed within the coal wall from the top to bottom, it is considered total failure. If the shape and distribution of maximum shear strain are uniformly distributed within the coal wall, but MSD is between 0 and 2 m, and

Table 3 Different modes of coal wall spalling based on MSD and LFSpI values

MSD (m)	LFSpI (%)	Spalling mode	Failure characteristics
0–3	0–40	Skin	Small chunks spalling out of coal wall Favourable for mining
	40–70	Blocky	Boulders like coal mass spalling out of coal wall May block the AFC
2–3	> 70	Total or fragmented	Total collapse of coal wall, either at once or like debris flow The shape of the coal wall is distorted
> 3	0–40	Skin or blocky	May or may not be favourable to AFC conveyance
	40–70	Blocky or fragmented or combination of both	Boulder size coal mass spalling out of coal wall or heap of fragmented coal mass flowing out of coal wall
	> 70	Total or blocky or fragmented or combination of two of three or combination of all three	Detrimental scenario of coal wall spalling Total collapse of the coal wall expected

LFSpI is between 0 and 40 %, then the spalling mode may be skin or chunk type of failure. Similarly, if the distribution of maximum shear strain within the coal wall is staggered with LFSpI between 40 and 70 % and MSD 0–3 m, blocky failure is anticipated. This classification system is purely depending upon the observations made in the simulation results obtained from the parametric study. This classification system can be effectually used for preparing a control strategy for coal wall spalling prior to the MWP.

The main roof weighting interval (MRWI) recorded at the MWP and the average shield loading in the mid zone were used to calibrate the numerical model. The MRWI is the distance between the setup room and the shield location during the MWP's main fall or main roof rupture. As indicated in Fig. 16, the MWP commenced at 77 m and completed at 83 m of face progress in the field. The MWP commenced at 78 m in the numerical simulation model, and the main fall occurred at 80 m of shield advance from the setup room. The field observations of the main roof caving interval and the computational model are very similar. The MWP phenomena may also be seen in the loading of the shields, as evident in Fig. 16. The shield loads were tracked in real time using a programmable mining controller-roof support (PMC-R) device with sensors that recorded the load and its progress. The longwall visual analysis (LVA) software was used to visualise the recorded shield loads. The longwall face shields were separated into three categories: main gate side (shield no. 1–36), mid zone (shield no. 37–110), and tail gate side (shield no. 111–146). The shield load corresponding to the mid zone was averaged and displayed versus the load computed numerically (Fig. 16). Peak load was reached at 78 m and dropped considerably at 80 m of face retreat, according to the numerically computed load. This explains that the MWP began at 78 m and ended with the main roof falling at 80 m of face retreat in the numerical model. The peak load was attained at 77 m and then considerably reduced around

83 m of face retreat, according to the field observed load measurement. As a result, it is reasonable to assume that the MWP began at 77 m and ended at 83 m of face retreat in the field. Shield loading behaviour in the field and numerically derived results showed a similar pattern.

4 Modelling Results and Discussion

4.1 Vertical Stress Distribution

Since the stress ratio (horizontal stress/vertical stress) is less than one in the field and in the model, vertical stress is considered to have a higher influence on coal wall spalling of the ALP longwall face. As previously stated, the failure of a coal wall is caused by the loss of confinement and excessive abutment stress due to excavation. While loss of confinement is unavoidable, understanding vertical stress superimposition or build-up at the longwall face can aid in the prevention or management of coal wall spalling. Figure 17 depicts the dynamic change in vertical stress surrounding the excavation with regard to face advancement. Figure 17 depicts the formation of elliptical stress relief zones surrounding the excavation, as well as stress concentration zones ahead of the longwall face. The size of stress relief zones grew in proportion to the length of the excavation. For example, when the face proceeded from setup room (0 m) to 10 m, 40 m, 69 m, 79 m, and 80 m, the height and width of the stress relief ellipse increased from 11.2 m, 24 m, 65.5 m, 93.4 m, 97.5 m, and 95.5 m and from 5 m, 16 m, 47 m, 78 m, 92 m, and 93 m, respectively. The height and width of the stress relief ellipse were 97.5 m and 92 m, respectively, at the peak stress phase, which occurred at 79 m of face advance when the longwall face encountered the highest amount of abutment stress. The height and width of the stress relief ellipse were 95.5 m and 93 m, respectively, when the main caving or mainfall of the main roof occurred. This implies that when the mainfall occurred, failure in the coal wall intensified, as demonstrated by the increase in the width of the stress relief ellipse.

With progressive face advancement, the vertical stress distribution in the coal wall was monitored. The vertical stress distribution in the coal wall up to 20 m ahead with face progress is depicted in Fig. 18. As the face advanced, the abutment vertical stress in the coal wall grew concurrently (Fig. 17). The highest value of abutment vertical stress was determined to be 14.8 MPa, 20.7 MPa, 31.6 MPa, 35.6 MPa, 42.7 MPa, and 39.7 MPa as the face moved from 0 to 10 m, 40 m, 69 m, 79 m, and 80 m, respectively. The maximal abutment vertical stress values were 1.4, 2, 3.1, 3.5, 4.2, and 3.9 times more than the premining vertical stress. As the face progresses, the excavation void increases, causing an increase in superimposed
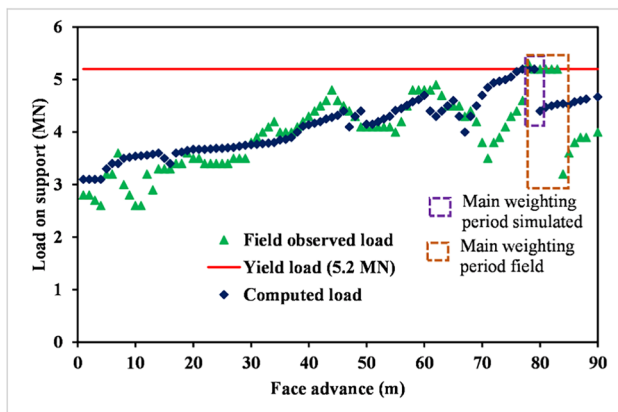

Fig. 16 Field-recorded shield load versus numerically computed shield load
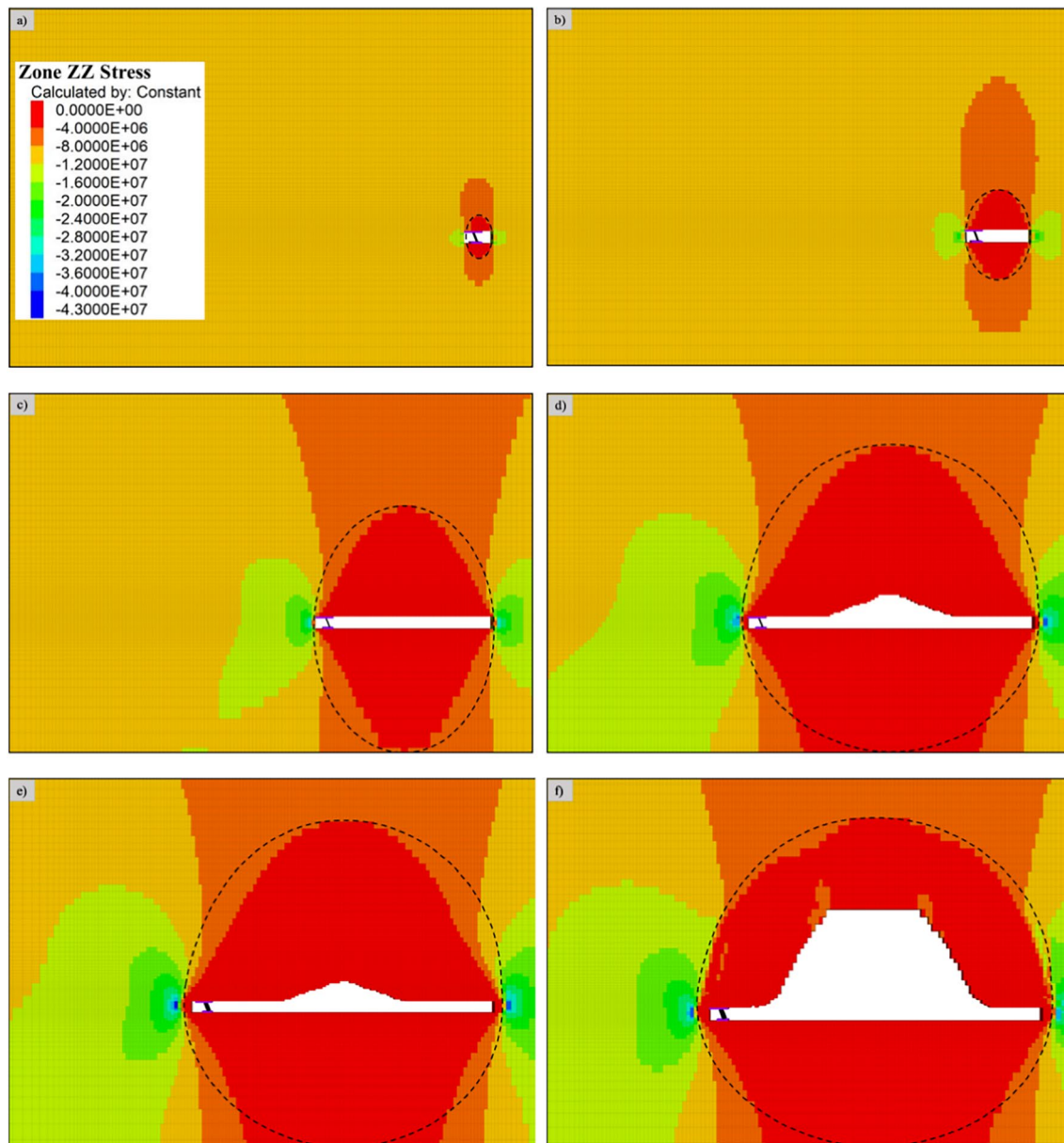
Fig. 17 Vertical stress distribution with progressive advance of face

vertical stress in the coal wall. Furthermore, Fig. 18 shows that the peak values of abutment vertical stress migrate farther away into the coal wall as the face proceeds. Peak vertical abutment stress is located at 1 m, 1 m, 2 m, 3 m, 4 m, and 4 m of face advance for 0 m, 10 m, 40 m, 69 m, 79 m, and 80 m of face advance, respectively. This implies that as the face progresses, the width of failure or yield in the longwall face increases. Another thing to consider is that as the face proceeds, the initial part of the coal wall loses its stress bearing capability, as seen in Fig. 18 by looking at the initial portion of the stress curve legends. For example, the initial value of vertical stress within 0–1

m in the coal wall for face advancement of 0 m, 10 m, 40 m, 69 m, 79 m, and 80 m is 13.6 MPa, 11 MPa, 7.2 MPa, 1.3 MPa, 0.01 MPa, and 0 MPa, respectively. Furthermore, at 79 m and 80 m of face advancement, which correspond to the panel's peak stress phase and mainfall phase, the initial slopes of the stress curve have become almost horizontal up to 2 m and 3 m into the coal wall. This indicates that the coal wall may spall up to 2 m and 3 m at the peak stress and mainfall phases, respectively. Furthermore, with face advancement, the vertical stress curve initially increases to its peak then gradually drops and becomes equal to the premining stress at some distance ahead into the coal wall.
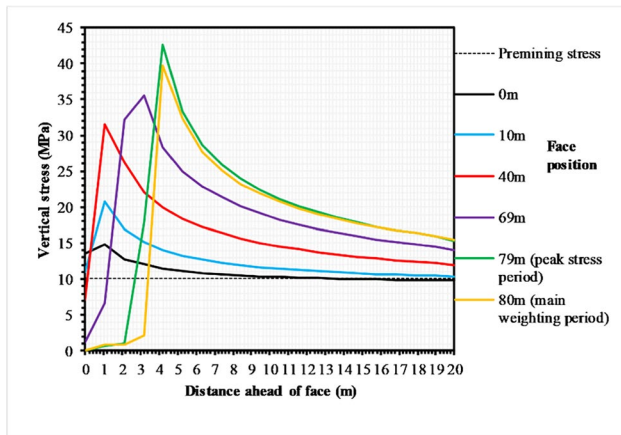
Fig. 18 Vertical stress distribution ahead of longwall face line

4.2 Material Failure

The failed region in and around the longwall face aids in defining its instability since they are stress relieved zones that have undergone substantial yielding. The length of the failed section in the coal wall is referred to as the extent of yield (EoY). The EoY was monitored with progressive face advancement. The number of FLAC[3D] elements yielded was also tracked, as was the nature or mode of yielding.

The yielding of FLAC[3D] elements surrounding the excavation acquired an elliptical shape. This elliptical-shaped region represents the zone of stress relief or the excavation-induced yield zone (EIYZ). EIYZ's width and height increased as the excavation progressed. For example, when the face proceeded from 0 to 10 m, 40 m, 69 m, 79 m, and 0 m, the height and width of the EIYZ increased from 7.9 m, 10.9 m, 23.6 m, 32.6 m, 37.3 m, and 44.9 m and 11 m, 21 m, 52 m, 82 m, 95 m, and 98 m, respectively (Fig. 19a–f). The width and height of EIYZ increased in a linear fashion as the face advanced. However, during the main fall phase, which occurred following the peak stress phase, the strata around the longwall excavation experienced substantial stress relaxation due to material failure. The immediate roof mainly failed in shear mode; however, the main roof above the excavation void failed in tension mode. Moreover, the main roof ahead of the longwall face failed in shear.

The EoY ahead of the longwall face showed a similar tendency of increasing with face progress. EoY was discovered to be between 1 and 2m throughout the earliest stages of excavation (1–47 m). EoY increased to 3 m between 48 and 72 m of face advance. Following that, EoY increased to 4m between 73 and 78 m, right before the MWP. EoY was 4 m at the peak stress phase, which was 79 m of face advance. EoY increased to 5 m when the mainfall phase occurred, i.e. 80 m of face progress. It can be said that during the MWP, a large amount of load is transferred to the coal wall. As a

result, the amount of spalling in the coal wall was at its peak during mainfall. Following the end of the MWP, an EoY of 3 m was detected at 81 m of face advance. This shows that avoiding face advance stoppage is the key to controlling failure at the longwall face.

As seen in Fig. 20, the nature or mode of failure of the coal wall was largely shear failure. Less than 18 FLAC[3D] elements failed in tension. Furthermore, tensile failure occurred at the top corner of the coal wall after 73 m of face advancement. The number of FLAC[3D] elements that failed in shear in the coal wall, on the other hand, increased with face progress, peaking during the mainfall phase. This adds to the fact that coal wall spalling is higher during the mainfall period. Within 5 m of EoY in the coal wall, about 128 FLAC[3D] elements failed in shear. It implies that 91.4 % of FLAC[3D] elements failed in shear within 5 m of EoY in the coal wall. Due to the high stress environment at 406.5 m depth, shear failure clearly dominated tensile failure in the coal wall.

4.3 Coal Wall Spalling

As previously described in section 3.5, three criteria were used in tandem to designate the zone of spalling in the coal wall: vertical stress distribution, maximum shear strain, and residual cohesion. Because of the formation of macroscale fractures, the spalling section of the coal wall is no longer capable of bearing vertical stress. In other words, the rock mass strength properties of the probable spalling region have deteriorated significantly or irreversibly. The gradual rise or near horizontal slope of the vertical stress distribution in the coal wall distinguishes it. The near flat slope of vertical stress distribution in the coal wall extends up to 3m, as shown in Fig. 21a. Furthermore, another acceptable coal wall spalling estimate criteria, maximum shear strain, reveals the localization of irreversible high plastic strain where considerable plastic flow occurs. It is one of the most dependable indicators for predicting shear fractures in coal wall. As a result, FLAC[3D] elements with maximum shear strains greater than the critical shear strain (0.09 in this study) are considered spalled. According to Fig. 21a, the extent of spalling extends up to 3 m up to the part of the coal wall where maximum shear strain exceeds 0.09. Cohesion greatly decreases in the area of the coal wall prone to spall due to extensive fracturing. Significant yielding and stress relaxation occur in the zone of spalling in the coal wall where cohesion has become negligible or zero. As far as a physical viewpoint of a fractured rock is concerned, such a criteria appears realistic. A typical shear test of a rock specimen indicates that when the specimen fractures, it loses cohesion along the fracture and its residual strength may be attributed purely to friction across the fracture surface. As a result, a simple criterion is presented in which the
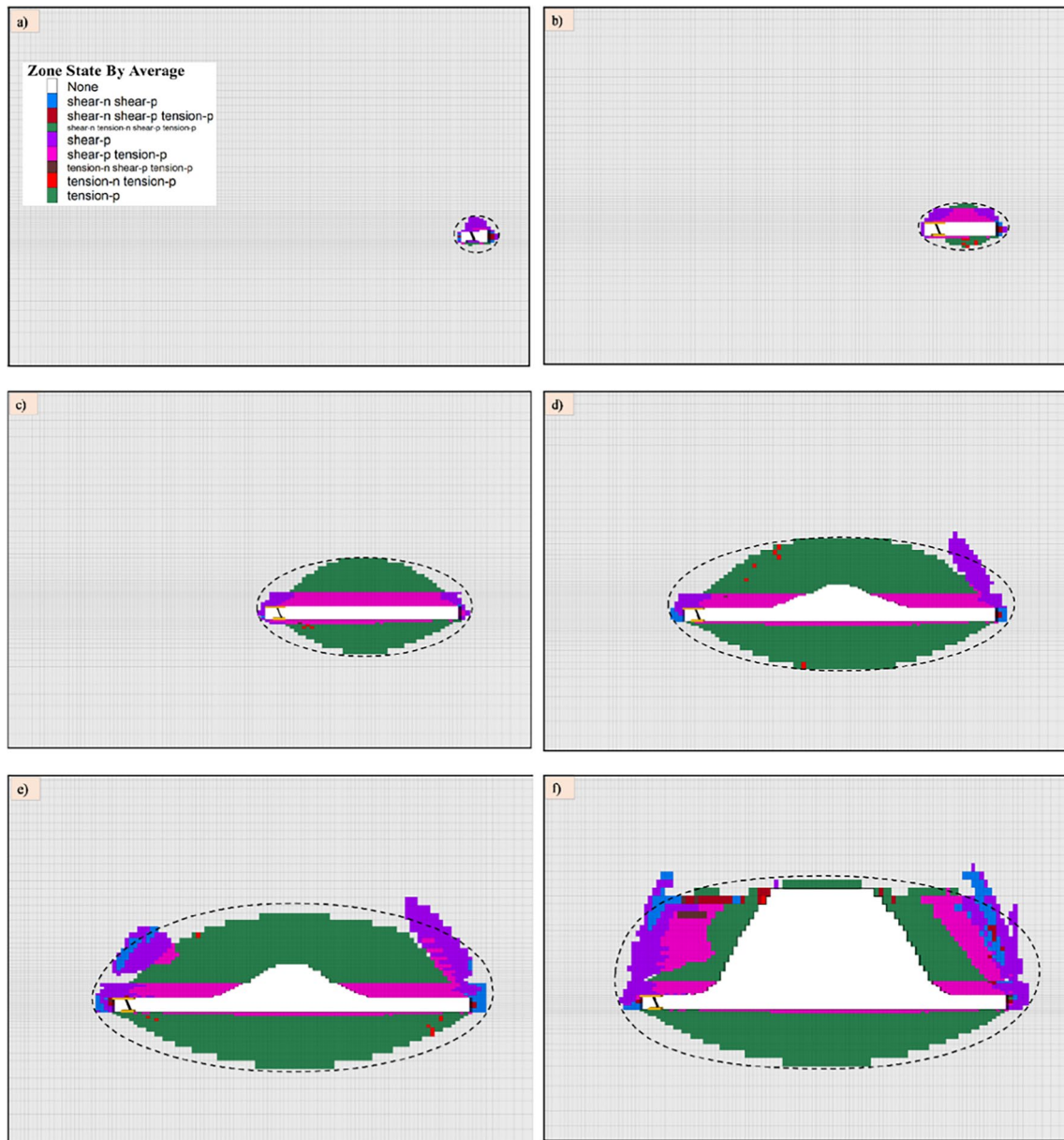
Fig. 19 Failure of FLAC^{3D} elements around the excavation void

extent of a coal wall spalling may be assessed by evaluating zones with cohesion less than 0.05 MPa. Based on cohesion criterion, the extent of spalling of coal wall is estimated as 3 m (Fig. 21b).

MSD refers to the extent of spalling, which in this case is 3 m. LFSpI, as defined in section 3.5, can be used to indicate the volume of coal wall spalled. The overall number of FLAC^{3D} elements prone to spall is 76, whereas the total number of FLAC^{3D} elements within 3 m of MSD is 84. As a result, the LFSpI is 90.5 %. According to Table 1, the predicted spalling mode in this scenario is total or fragmented failure. Spalling in the field extended from the floor to the

complete height of coal wall. However, the majority of the spalling emanated from the top section of the coal wall. Furthermore, the mode of failure in ALP was fragmented, with big boulder-sized to small fragmented coal spalling out of the coal wall, as seen in Fig. 9. As a result, the numerical modelling could appropriately estimate spalling of the coal wall for the ALP mine.

Figure 22 shows the number of FLAC^{3D} elements that spalled off the coal wall as the face advanced. In general, coal wall spalling commenced when the face proceeded to 49 m from the setup room. There was no spalling in the coal wall for the first 1–48 m of face progress. MSD of 1 m was measured between 49 and 64 m, with
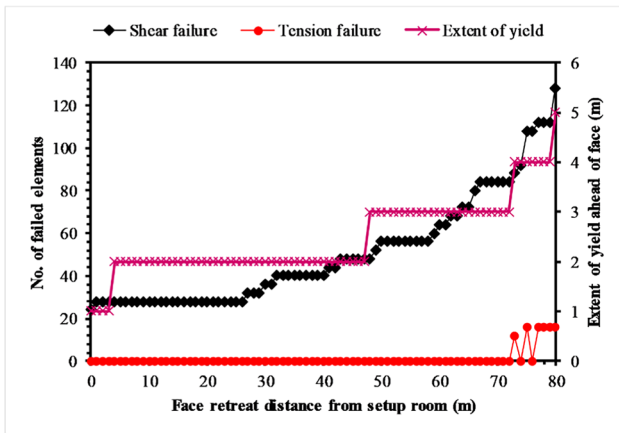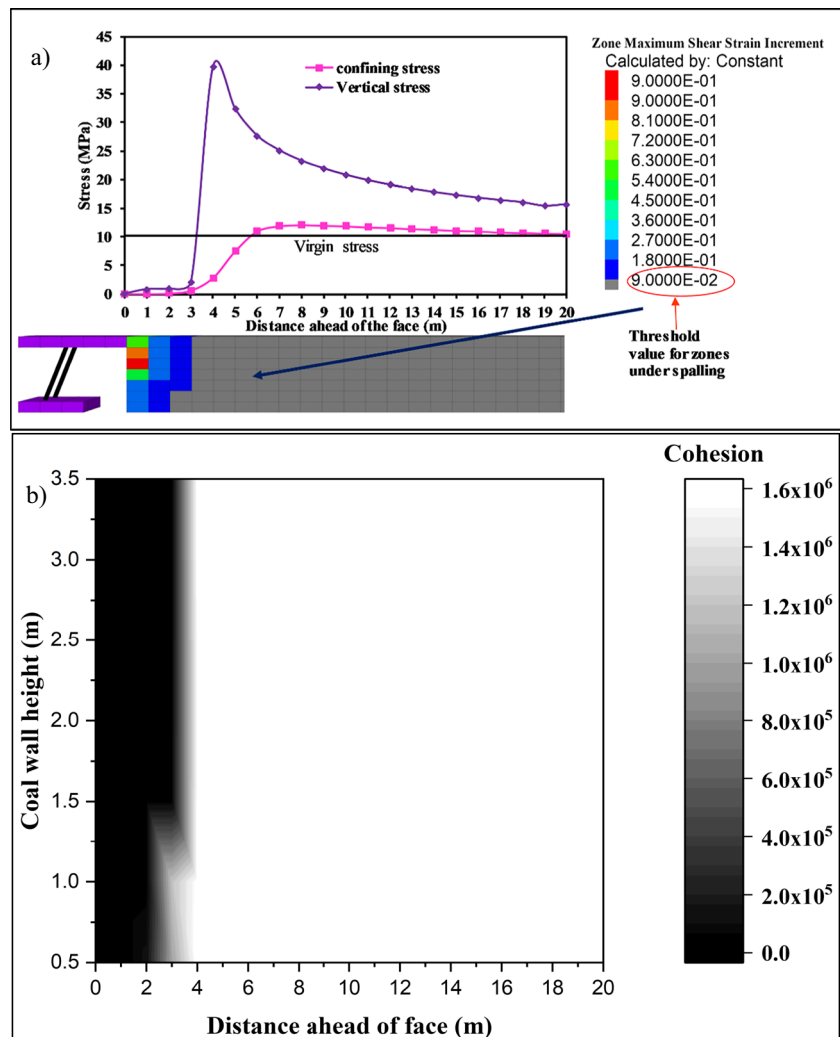
Fig. 20 Mode of failure and extent of failure in the coal wall

LFSpI ranging from 15 to 100 %. It implies that the spalling of the coal wall was advantageous to the mining operation and did not cause too many problems. MSD of 2 m was reported at 65–78m

with LFSpI values greater than 58 %. Several times during this period, coal wall spalling seemed to obstruct the AFC. Furthermore, during the MWP, 3 m MSD was measured with LFSpI of 87 and 90.5 %, respectively. The integrity of the coal wall was compromised, resulting in AFC obstruction. The longwall face operation was put on hold until the clearance work was finished.

5 Effect of Roof Properties on Coal Wall Spalling

5.1 Field Compressive and Tensile Strength of Immediate Roof

The values chosen for evaluating the influence of immediate roof compressive strength (Scir) reflect weak to strong strata and are 3.5 MPa, 5.8 MPa, 8.6 MPa, and 12.9 MPa. MSD increased significantly when Scir increased. For instance, as Scir increased from 3.5 to 12.9 MPa, MSD increased from 6.4 m, 12.7 m, 14.3 m, and 14.5 m, respectively (Fig. 23).
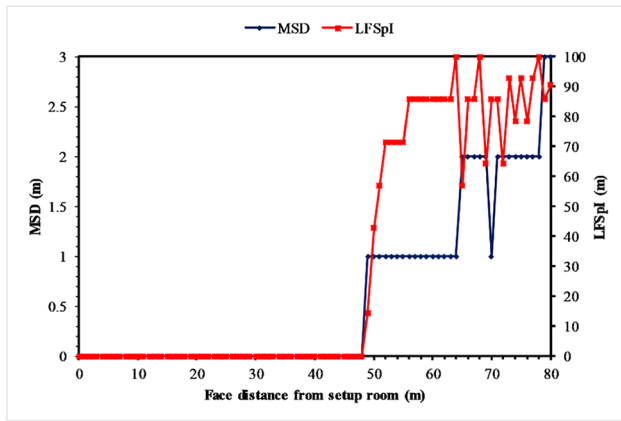
Fig. 21 Spalling estimation of coal wall for ALP, panel 1 face

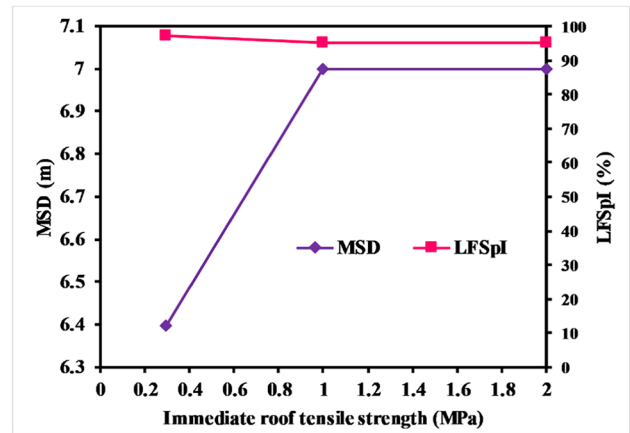**Fig. 22** Spalling of coal wall with progressive face advance in ALP, panel 1

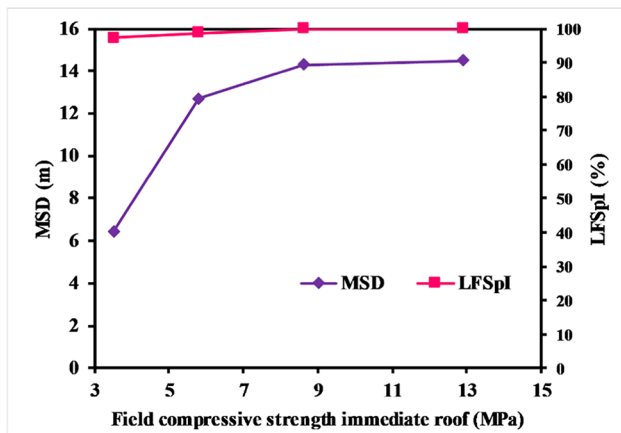**Fig. 23** Impact of compressive strength of immediate roof on coal wall spalling

Fig. 24 Impact of tensile strength of immediate roof on coal wall spalling

result, it is recommended that caving of the immediate roof be monitored and overhang avoided.

In contrast, increasing the field tensile strength of the immediate roof (Stir) from 0.3 to 1 MPa and 2 MPa seemed to have little influence on coal wall spalling (Fig. 24). The reason for this is that the caving of immediate roof is governed by shear mode of failure at depth below 400 m. With increased Stir, only a 10 % difference in MSD values was seen. The LFSpI remained quite steady. The PFAVS value increased slightly from 26.8 to 27.7 MPa, correlating to a 0.6 m increase in MSD.

5.2 Field Compressive and Tensile Strength of Main Roof

The main roof compressive strength (Scmr) was varied from 4.3 to 7.7 MPa and 12.9 to 15.4 MPa, and the change in MSD and LFSpI was recorded. MSD was found to steadily rise for the first three variations. For example, when Scmr was increased from 4.3 to 12.9 MPa, MSD increased from 6.4 to 6.8 to 7 m (Fig. 25). The overall increase in MSD was less than 10%. However, when Scmr was increased to 15.4 MPa, MSD increased significantly to 12.8 m. Furthermore, for all Scmr changes, PFAVS were 26.8 MPa, 26.9 MPa, 27 MPa, and 27.5 MPa, respectively. In addition, EoY ranged from 8 to 12 m and 15 to 17 m. For all Scmr variations, LFSpI declined linearly from 97.2, 90, 76.2, to 65.4 %. According to the findings, the extent of spalling depth increased, while the region of spalling shifted from full height to the top portion of the coal wall. Overall, the spalling of the coal wall increases with increasing Scmr as the number of FLAC³ᴰ elements under spalling increases from 140, 108, 152, to 196. The overall increase in coal wall spalling can be linked to the delay in main roof caving as MRWI extended from 46 to 70 m of face advance. There
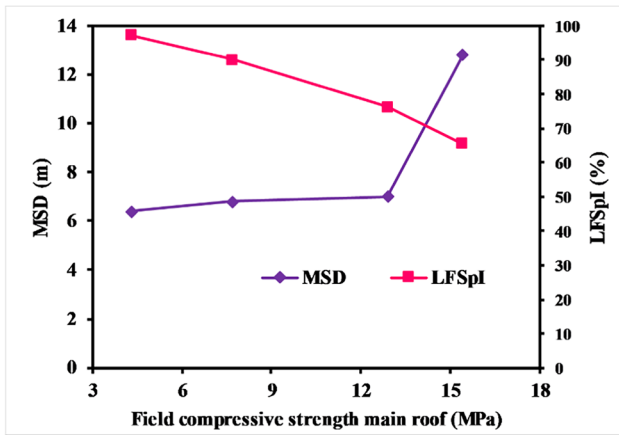
The overall percentage increase in MSD with regard to the 3.5 MPa Scir model was 98.4 %, 123.4 %, and 126.6 %, respectively. Peak front abutment vertical stress (PFAVS) values found were 26.8 MPa, 29.5 MPa, 33.3 MPa, and 34.8 MPa, respectively. Furthermore, EoY extended from 8 m to 14 m, 15 m, and 16 m. When Scir was increased, LFSpI showed minimal change. For instance, with a change in Scir values, LFSpI increased from 97.2 to 98.7 %, 100 %, and 100 %. Furthermore, the coal wall's failure mode was shear. It suggests that Scir's contribution is critical in causing instability in the coal wall. If the MSD is greater than 3 m and the LFSpI is greater than 70% at depths more than 400 m, the scenario is detrimental and indicates fragmented or total type of coal wall failure. [37] reported similar results. They discovered that increasing the Scir of the immediate roof created considerable overhang behind the shield, hence increasing the PFAVS in the coal wall. As a

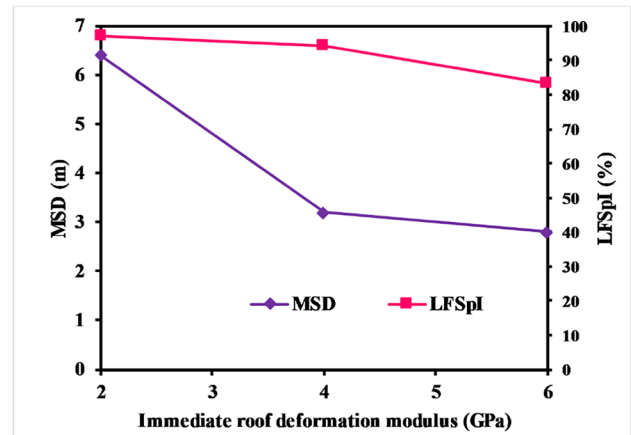**Fig. 25** Impact of compressive strength of main roof on coal wall spalling

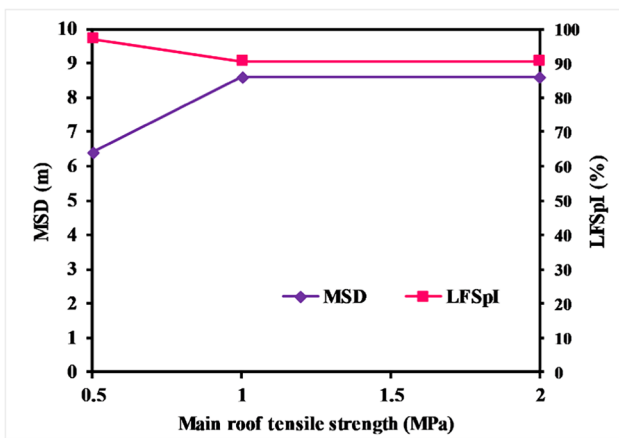**Fig. 27** Impact of immediate roof deformation modulus on coal wall spalling

Fig. 26 Impact of tensile strength of main roof on coal wall spalling

might be two corrective procedures to reduce face instability in this situation. To begin, make good use of the powered support's face sprag board, which gives confinement to the upper portion of the coal wall, and second, to artificially induce caving of the main roof in order to lessen the stress accumulation in the face.

The main roof's field tensile strength (Stmr) was varied from 0.5 to 2 MPa. MSD rose from 6.4 to 8.6 m when Stmr was increased from 0.5 to 1 MPa (i.e. approximately 34.4%). It stayed unaltered after that (Fig. 26). On the other hand, LFSpI remained rather static, with values of 97.2 %, 90.7 %, and 90.7 % for all variations of Stmr. As a result, while increasing the Stmr may increase the depth of spalling in the coal wall, the area of spalling stays relatively unaltered. This shows that the cavability of the main roof and the amount of coal wall spalling are highly correlated. The main roof above the excavated void appears to fail in tension mode. However, the main roof ahead of the longwall face failed in

shear mode. Increasing the Stmr delayed the main roof initial caving since the MRWI reported was 46 m, 48 m, and 48 m. Due to the delay in caving of the main roof, the PFAVS rose from 26.8 to 28.2 MPa for all Stmr variations.

5.3 Deformation Modulus of Immediate Roof and Main Roof

Three models were created using three different values (2 GPa, 4 GPa, and 6 GPa) of the deformation modulus of the immediate roof (Ei), and their impact on coal wall spalling was noted. As illustrated in Fig. 27, MSD appeared to decrease from 6.4 to 3.2 to 2.8 m with increasing Ei values. The total percentage reduction in MSD compared to the 2 GPa model is 50% and 56.3 %, respectively. The initial increase in Ei from 2 to 4 GPa resulted in a 50 % decrease. Following that, only a 6.3 % difference in MSD decrease percentage was noticed. However, despite an increase in total PFAVS from 26.8 to 27.6 to 27.8 MPa, EoY decreased from 8 to 5 to 4 m. As a result, the LFSpI values decreased from 97.2 to 94.4 to 83.3 %. It implies that an increase in PFAVS does not always imply an increase in EoY. Spalling is reduced since the horizontal deformation of the coal wall is a direct result of the vertical displacement of the immediate roof. As Ei increases, the immediate roof becomes less prone to vertical displacement. As a result, the coal wall's horizontal displacement was decreased. This is a reasonable explanation that has been confirmed by other studies [1, 7]. In all cases of Ei, the values of MSD and LFSpI together indicate total or fragmented failure.

As shown in Fig. 28, sensitivity analysis was performed for three alternative values of the main roof deformation modulus (Em). LFSpI appears to be quite stable, ranging between 94.4 and 100 %, resembling total or integral failure. MSD, on the other hand, increased from 6.4 to 7.9 m.
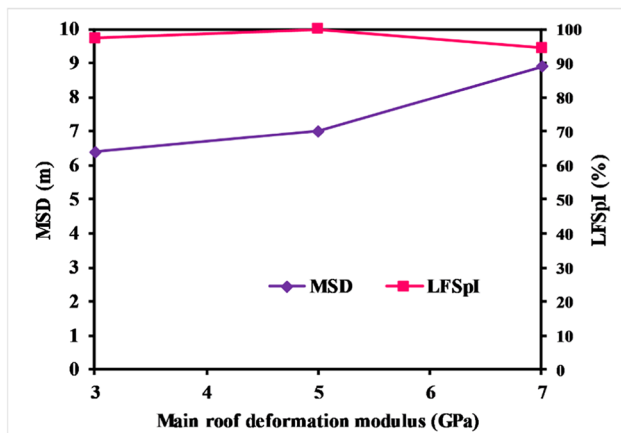
Fig. 28 Impact of main roof deformation modulus on coal wall spalling

The total percentage increase in MSD compared to the 3 GPa model is 9.4 % and 39.1 %, respectively. Furthermore, PFAVS rose from 26.8 to 27.6 MPa and then to 28.1 MPa. Furthermore, EoY extended from 8 to 10 to 11 m. It signifies that increasing Em causes the coal wall to spall increasingly. Because of the increase in Em, MRWI increased dramatically from 46, 57, to 64 m. It denotes delayed caving of the main roof, which increases the stress on the face. As a result, artificial caving of the main roof is proposed to provide stress relief at the face.

6 Summary and Conclusion

FLAC^{3D} was used in this work to simulate panel 1 based on geological data from the Adriyala Longwall Project (ALP) mine. The study's major goal was to outline coal wall spalling during the main weighting period (MWP) in detail. As a result, main aspects (vertical stress distribution, material failure, and actual spalling estimation) of coal wall instability owing to progressive panel excavation were investigated. For the area of interest, the simulation effectively integrated strain-softening constitutive rule. Furthermore, an algorithm was developed for accurately capturing the caving behaviour of roof beds, shield advancement, and coal extraction. The main roof weighting interval (MRWI) and load coming onto the shields were used to calibrate the numerical model for the ALP mine. Furthermore, the impact of roof bed geotechnical features on coal wall spalling was investigated. The current investigation leads to the following findings:

The superimposition of vertical stress is critical in determining coal wall instability. In both the vertical and horizontal directions, an elliptical stress relief zone was formed. The length of the excavation determined the size of the stress relief zone. During the peak stress phase, the height of the stress relief zone is greatest, whereas the width is highest during the main fall phase. The peak front abutment vertical stress (PFAVS) increased with progressive face advancement until the peak stress phase then declined during the main fall phase. As mining progressed, the location of PFAVS shifted further away from the face line into the coal wall. As the face progresses, the initial portion of the coal wall begins to lose its stress-bearing capability.

The distribution of yielded FLAC^{3D} elements around the excavation void was likewise elliptical in shape. The immediate roof mostly caved in shear, but the main roof above the excavation void collapsed in tension. Furthermore, the main roof ahead of the longwall face failed in shear. Until the MWP was over, the extent of yield (EoY) ahead of the longwall face increased with face advancement. During the MWP, the maximum EoY in the coal wall was 5 m. Shear failure dominated the failure mechanism of FLAC^{3D} elements in the coal wall.

Spalling was evaluated based on three distinct criteria: vertical stress distribution, maximum shear strain, and residual cohesion of coal wall. To quantify coal wall spalling, the maximum spalling depth (MSD) and longwall face spalling index (LFSpI) were established. During the MWP, panel 1 of the ALP mine recorded an MSD of 3m and an LFSpI of 90.5%. Total or fragmented failure was the expected spalling mode for ALP, which complemented the field observation well.

The compressive strength of the immediate roof seemed to have a substantial impact on coal wall spalling, according to the research. The tensile strength of the immediate roof appeared to have minimal effect on coal wall spalling.

Only until the compressive strength of the main roof achieved 15.4 MPa did the spalling of the coal wall appears to increase significantly. However, increasing the main roof's tensile strength from 0.5 to 1 MPa appears to increase coal wall spalling. After that, even when the main roof's tensile strength was increased to 2 MPa, spalling of the coal wall continued unaffected.

Spalling of the coal wall appears to be reduced significantly when the deformation modulus of the immediate roof is increased. On the other hand, increasing the deformation modulus of the main roof delayed the onset of initial caving of the main roof, resulting in increased coal wall spalling.

The findings of the suggested numerical simulation exercise can enable strata control engineers better recognise the risks of coal wall spalling and improve face control for a safe and productive longwall face operating environment.

As a result, the findings and opinions expressed are those of the authors and not necessarily, those of the organisation they serve.

Author Contribution Sunny Murmu was involved in conceptualization, software, simulation, and manuscript drafting. Gnananandh Budi was involved in supervision, editing, and proof reading.

Data Availability Some or all data, models, or code that support the findings of this study are available from the corresponding author upon reasonable request.

Declarations

Competing Interests The authors declare no competing interests.

References

1. Barczak TM, Chase FE, Organiscak JA (1993) Longwall face stability : an evaluation of face sloughage

2. Bai QS, Tu SH, Chen M, Zhang C (2016) Numerical modeling of coal wall spall in a longwall face. Int J Rock Mech Min Sci 88:242–253. https://doi.org/10.1016/j.ijrmms.2016.07.031

3. Murmu S, Budi G (2021) A probability-based risk assessment of roof strata weighting in longwall panels. Arbian J Geosci 14:362. https://doi.org/10.1007/s12517-021-06637-y

4. Singh GSP, Singh UK (2010) Numerical modeling study of the effect of some critical parameters on caving behavior of strata and support performance in a longwall working. Rock Mech Rock Eng 43:475–489. https://doi.org/10.1007/s00603-009-0061-1

5. Song G, Chugh YP, Wang J (2017) A numerical modelling study of longwall face stability in mining thick coal seams in China. Int J Min Miner Eng 8:35–55. https://doi.org/10.1504/IJMME.2017.082682

6. Pappas DM, Bauer ER, Mark C (2000) Roof and rib fall incidents and statistics: a recent profile. In: New technology for coal mine. Pittsburgh, USA, pp 3–21

7. Yong Y, Shihao T, Qi W et al (2011) Mechanics of rib spalling of high coal walls under fully-mechanized mining. J Min Sci Technol 21:129–133. https://doi.org/10.1016/j.mstc.2010.12.014

8. Bai Q, Tu S, Li Z, Tu H (2015) Theoretical analysis on the deformation characteristics of coal wall in a longwall top coal caving face. Int J Min Sci Technol 25:199–204. https://doi.org/10.1016/j.ijmst.2015.02.006

9. Guo WB, Liu CY, Dong GW, Lv WY (2019) Analytical study to estimate rib spalling extent and support requirements in thick seam mining. Arab J Geosci 12. https://doi.org/10.1007/s12517-019-4443-8

10. Jiachen W, Shengli Y, Dezhong K (2016) Failure mechanism and control technology of longwall coalface in large-cutting-height mining method. Int J Min Sci Technol 26:111–118. https://doi.org/10.1016/j.ijmst.2015.11.018

11. Li XP, Kang TH, Yang YK et al (2015) Analysis of coal wall slip risk and caving depth based on Bishop Method. J China Coal Soc 40:1498–1504

12. Liu S, Yang K, Zhang T, Tang C (2020) Rib spalling 3D model for soft coal seam faces with large mining height in protective seam mining: Theoretical and Numerical Analyses. Geofluids 2020. https://doi.org/10.1155/2020/8828844

13. Wang J, Wang Z (2019) Systematic principles of surrounding rock control in longwall mining within thick coal seams. Int J Min Sci Technol 29:65–71. https://doi.org/10.1016/j.ijmst.2018.11.014

14. Tian M, Han L, Xiao H, Meng Q (2021) Experimental study of deformations and failures of the coal wall in a longwall working

face. Eng Fail Anal 125:105428. https://doi.org/10.1016/j.engfailanal.2021.105428

15. Wang S, Wu X, Zhao Y, Hagan P (2018) Mechanical performances of pressure arch in thick bedrock during shallow coal mining. Geofluids 2018:1–13. https://doi.org/10.1155/2018/2419659

16. Yang S, Song G, Kong D (2019) An evaluation of longwall face stability in thick coal seams through a basic understanding of shield-strata interaction. J Geophys Eng 16:125–135. https://doi.org/10.1093/jge/gxy011

17. Yongxiang XU, Guofa W, Mingzhong LI et al (2021) Investigation on coal face slabbed spalling features and reasonable control at the longwall face with super large cutting height and longwall top coal caving method. J China Coal Soc 46:357–369

18. Bai Q, Tu S, Zhang X (2013) Numerical modeling on brittle failure of coal wall in longwall face — a case study. Arab J Geosci 7:5067–5080. https://doi.org/10.1007/s12517-013-1181-1

19. Kong DZ, Cheng ZB, Zheng SS (2019) Study on the failure mechanism and stability control measures in a large-cutting-height coal mining face with a deep-buried seam. Bull Eng Geol Environ 78:6143–6157. https://doi.org/10.1007/s10064-019-01523-0

20. Song G, Chugh YP (2018) 3D analysis of longwall face stability in thick coal seams. J South African Inst Min Metall 118:131–142. https://doi.org/10.17159/2411-9717/2018/v118n2a6

21. Yao Q, Li X, Sun B et al (2017) Numerical investigation of the effects of coal seam dip angle on coal wall stability. Int J Rock Mech Min Sci 100:298–309. https://doi.org/10.1016/j.ijrmms.2017.10.002

22. Behera B, Yadav A, Singh GSP, Sharma SK (2021) Assessment of excavation damage and spalling potential at a mechanized longwall face: a numerical modeling study. Geomech Geophys Geo-Energy Geo-Resources 7:104. https://doi.org/10.1007/s40948-021-00299-6

23. Guo W, Zhao G, Bai E et al (2021) Effect of overburden bending deformation and alluvium mechanical parameters on surface subsidence due to longwall mining. Bull Eng Geol Environ 80:2751–2764. https://doi.org/10.1007/s10064-020-02091-4

24. Sui W, Hang Y, Ma L et al (2015) Interactions of overburden failure zones due to multiple-seam mining using longwall caving. Bull Eng Geol Environ 74:1019–1035. https://doi.org/10.1007/s10064-014-0674-9

25. Xueyi Y, Xuwei M (2020) A preliminary discrimination model of a deep mining landslide and its application in the Guanwen coal mine. Bull Eng Geol Environ 79:485–493. https://doi.org/10.1007/s10064-019-01565-4

26. Sheorey PR, Mohan GM, Sinha A (2001) Influence of elastic constants on the horizontal in situ stress. Int J Rock Mech Min Sci Geomech Abstr 38:1211–1216

27. Satyanarayana I, Budi G, Murmu S (2021) Stability analysis of a deep highwall slope using numerical modelling and statistical approach—a case study. Arab J Geosci 14:1–12. https://doi.org/10.1007/s12517-021-06476-x

28. Zhang L (2010) Estimating the strength of jointed rock masses. Rock Mech Rock Eng 43:391–402. https://doi.org/10.1007/s00603-009-0065-x

29. Zhang L, Einstein HH (2004) Using RQD to estimate the deformation modulus of rock masses. Int J Rock Mech Min Sci 41:337–341. https://doi.org/10.1016/S1365-1609(03)00100-X

30. Salamon MDG, Munro AH (1967) A study of the strength of coal pillars. J S Afr Inst Min Met 68:55–67

31. Agrawal A, Choudhary BS, Murthy VMSR, Murmu S (2022) Impact of bedding planes, delay interval and firing orientation on blast induced ground vibration in production blasting with controlling strategies. Meas J Int Meas Confed 202:111887. https://doi.org/10.1016/j.measurement.2022.111887

32. Maheshwari P, Murmu S, Verma HK (2019) Modeling of blast induced damage distance for underground tunnels. Indian Geotechnical Conference, pp 617–626

33. Murmu S, Maheshwari P, Verma HK (2018) Empirical and probabilistic analysis of blast-induced ground vibrations. Int J Rock Mech Min Sci 103:267–274. https://doi.org/10.1016/j.ijrmms.2018.01.038

34. Murmu S, Budi G (2022a) Analysis of failure associated with longwall face during the main weighting period using a numerical modelling approach. Min Technol 131:1–18. https://doi.org/10.1080/25726668.2022.2082152

35. Murmu S, Budi G (2022b) Study on the mechanism, prediction, and control of coal wall spalling in deep longwall panels utilizing advanced numerical simulation methodology. Geofluids 2022:1–19. https://doi.org/10.1155/2022/5622228

36. Shabanimashcool M, Li CC (2012) Numerical modelling of longwall mining and stability analysis of the gates in a coal mine. Int J Rock Mech Min Sci 51:24–34. https://doi.org/10.1016/j.ijrmms.2012.02.002

37. Singh GSP, Singh UK (2009) A numerical modeling approach for assessment of progressive caving of strata and performance of hydraulic powered support in longwall workings. Comput Geotech 36:1142–1156. https://doi.org/10.1016/j.compgeo.2009.05.001